Nanoscale

ROYAL SOCIETY OF CHEMISTRY

PAPER

View Article Online
View Journal | View Issue

Cite this: *Nanoscale*, 2025, **17**, 2658

Theoretical insights into spacer molecule design to tune stability, dielectric, and exciton properties in 2D perovskites†

Xing Liu, Hejin Yan, Zheng Shu, Xiangyue Cui and Yongqing Cai *

Two-dimensional organic–inorganic perovskites have garnered extensive interest owing to their unique structure and optoelectronic performance. However, their loose structures complicate the elucidation of mechanisms and tend to cause uncertainty and variations in experimental and calculated results. This can generally be rooted in dynamically swinging spacer molecules through two mechanisms: one is the intrinsic geometric steric effect, and the other is related to the electronic effect *via* orbital overlapping and electronic screening. Herein, we design three types of spacer molecules, phenyl methyl ammonium (PMA), thiophene methyl ammonium (THMA), and furan methyl ammonium (FUMA), that adopt different aromatic units. We examine the influence of different aromatic spacers on the structural properties of the inorganic layer of the perovskite based on first-principles calculations and find that a marginal change in the aromatic ending group in the spacer ligand would trigger significant changes in the octahedral inorganic layer. We predict that using THMA and FUMA can improve the stability and increase the size of crystal domains because of enhanced binding between the organic and inorganic layers. Compared to the prototype phenyl-based perovskite $(PMA)_2PbI_4$, the thiophene-based perovskite $(THMA)_2PbI_4$ exhibits states closer to the band edge, thus boosting carrier transport across inorganic and organic layers. Compared with the perovskite using PMA as a spacer cation, the THMA-based perovskite demonstrates a higher dielectric constant and smaller exciton binding energy, suggesting that THMA is more suitable as an organic spacer and a good passivation agent in 3D perovskites. The difference in the screening ability of the molecules induces varying interlayer excitonic binding energy. Our work provides theoretical grounds for the engineering of spacer molecules toward high-efficiency light conversion of mixed perovskites.

Received 25th October 2024,
Accepted 30th December 2024

DOI: 10.1039/d4nr04406a

rsc.li/nanoscale

1. Introduction

Halide perovskites have garnered extensive interest considering their high light absorption coefficient,[1] high mobility,[2] long carrier lifetime and diffusion length,[3] defect-tolerant nature,[4] and tunable composition.[5] Their appealing optoelectronic properties make them promising candidates for a host of applications, such as solar cells,[6] light-emitting diodes,[7] field-effect transistors,[8] lasers,[9] and detectors.[10] In 2009, Miyasaka *et al.*[11] reported construction of solar cells based on hybrid organic–inorganic perovskites (HOIPs) for the first time, showing a power conversion efficiency (PCE) of 3.8%. By improving growth conditions for enhancing the crystalline quality of the material, record-breaking PCE values have been continuously reported, up to 26.1%, in recent years.[12] A host of three-dimensional (3D) HOIPs with the general formula AMX_3 (A = Cs^+, $CH_3NH_3^+$ (MA), and $HC(NH_2)^{2+}$ (FA); M = Pb^{2+}, Sn^{2+}, and Ge^{2+}; X = Cl^-, Br^-, and I^-) has been discovered and demonstrated various potential optoelectronic and energy-conversion applications.[4,13–16]

Thus far, considerable efforts have been devoted to the following aspects of research on halide perovskites: optimized compositions for improving PCE,[17] measures for promoting stability[18] and up-scaling synthesis of materials with satisfactory quality.[19,20] Mixed perovskites comprising several different types of cations and having a wide solar-adsorbing spectrum and high stability are particularly appealing. An ideal combination of different cations for synthesizing mixed perovskites has been proposed according to the charge transfer to its precursor PbI_2 using density functional theory.[21,22] Selectively adding long-chain organic cations into 3D perovskites is also effective in promoting the stability by triggering the formation of two-dimensional (2D) halide perovskites, with cleavage along specific crystal planes ⟨100⟩, ⟨110⟩, or ⟨111⟩ of bulk perovskites to form 2D perovskites or quasi 2D perovskites.[23] These molecules, acting as the spacer molecules,

Joint Key Laboratory of the Ministry of Education, Institute of Applied Physics and Materials Engineering, University of Macau, Macau SAR 999078, China.
E-mail: yongqingcai@um.edu.mo

† Electronic supplementary information (ESI) available. See DOI: https://doi.org/10.1039/d4nr04406a

effectively passivate and separate the cleaved Pb–I 2D layers while imposing significant quantum confinement for a tunable band gap. Importantly, by introducing different charged end groups in these spacer molecules, various interlayer stacking registries, such as Ruddlesden–Popper (RP)[24] Dion–Jacobson[25] and alternating cation interlayer (ACI)[26] phases, can be obtained, further extending the regulation of perovskite polymorphs.

Compared with 3D parent perovskites, 2D perovskites are believed to be more robust against moisture and oxygen and accordingly have high stability for the following reasons.[27] First, structural instability and phase transition in 3D perovskites driven by lattice strain and causing a strict restriction of ion radii, dictated by the tolerance factor, can be principally relieved and allow more phase freedom in 2D perovskites.[28] Second, the large organic cations can pin the lattice and decrease phase instability as steric hindrances.[29] Third, ion migration, resulting in a large number of defects in 3D perovskites and eventually the destruction of the perovskite skeleton and decomposition, can be inhibited by using large organic cations as barriers to isolate the octahedral layer in 2D perovskites.[30] Fourth, excessive layered PbI_2 in 3D perovskites can be reacted with large cations as a passivation agent, forming a 2D perovskite layer.[31] The MA/FA/I vacancies on the perovskite surface can also be filled with methylamine from a large organic cation, reducing the harmful defective states and nonradiative recombination.[32]

Moreover, 2D perovskites have excellent structural diversity, and their properties can be tailored by controlling the spacing cations,[33] cage cations,[34] and inorganic layer thickness.[35] However, the transport of charge carriers tends to be hindered by adding large cations.[36] The *n* value, the number of inorganic cationic (*i.e.*, Pb) sublayers forming a quantum well for carriers, dictates the width of the quantum well, while the length of organic cations determines the thickness of the quantum well barrier. Both of them can directly affect the transport process of charge carriers.[37] Since the dielectric constant of organic materials is significantly smaller than that of the inorganic Pb–I layer, a significant quantum confinement effect is expected in 2D perovskites.[38] This allows the generation of spatially confined excitons in the inorganic layer with the surrounding organic layer as a shielding layer of excitons.[39] Therefore, 2D perovskites inherent with a natural quantum well generally have a large exciton binding energy (E_b).[40] In principle, the E_b can be adjusted by modulating the dielectric constant of the spacer cations. Designing the spacer layer with a higher dielectric constant can reduce the dielectric mismatch between the organic and inorganic layers, thereby reducing E_b.[41] Therefore, large hydrophobic cations with high conductivity and dielectric screening are helpful in maintaining stability while ensuring a good transport performance of perovskites.

Aromatic organic ligands have a conjugated electronic structure, allowing relatively high dielectric constants and ideally act as spacer molecules to reduce the dielectric mismatch.[42] Due to its appropriate volume and easy modification, the aromatic benzene ring unit has become the most commonly used group in the spacer molecules.[43] In 2016, Kamminga *et al.* studied the effect of phenylamine cations with different lengths of fatty chains on the crystal structure of 2D perovskite.[44] Phenyl methyl ammonium (PMA) and phenylethylamine (PEA) molecules are found to be suitable as spacer cations for 2D perovskites. Yan *et al.* prepared and studied thin films, including PMA and its derivatives as spacer cations,[45] obtaining a dense perovskite film with a PCE of 17.12% and long-term stability. On the other hand, the thiophene organic ligand with an S atom in the aromatic ring exhibits a unique interaction with Pb,[46] and this interaction facilitates the amalgamation of adjacent grains and the passivation of I vacancies. Due to the high polarizability of sulfur atoms, valence π electrons are more loosely bound to the aromatic ring, resulting in higher charge mobility. In 2018, Liu *et al.*[47] prepared 2D perovskite films based on thiophene methyl ammonium (THMA) and methyl ammonium chloride (MACl) as additives, achieving significantly increased grain size and improved charge transfer. The 2D perovskite device has a perovskite solar cell (PSC) efficiency of 15.42% and exhibits superior long-term stability. Liu *et al.*[48] used THMA as an organic ligand and prepared the FA-based 2D perovskite. The optimized $(THMA)_2(FA)_4Pb_5I_{16}$-based device has a record efficiency of 19.06%. Ni *et al.*[49] compared thiophene-based and phenyl-based 2D perovskites and found that introducing THMA improved the charge transfer between the inorganic layer and the organic ligand, resulting in better photoelectric performance. Besides the spacer molecules featured with benzene ring and thiophene groups, furan molecules have also been adopted. Zheng *et al.*[50] used furan methylamine hydro (FUMA) iodate to prepare 2D PSCs and achieved a PCE of 15.24%. Liu *et al.*[51] reported that the 2D perovskite with FUMA ligand has an ultralong carrier lifetime and a PCE of 18.00% due to its lower exciton binding energy and electron–phonon coupling coefficient. Although many studies have focused on the inorganic layer, the role of spacer molecules in determining the electronic and excitonic properties of the whole 2D perovskites has received little attention. However, recent studies have highlighted the role of spacer molecules in influencing the structural, electronic, and optical properties of 2D perovskites. For instance, Marchenko *et al.*[52] constructed a database of two-dimensional hybrid perovskite materials, systematically analyzing their crystal structures and properties. Lu *et al.*[53] systematically explored the impact of metal off-centering distortion in halide perovskites by combining high-pressure experiments and first-principles calculations. Lyu *et al.*[54] developed a machine-learning-assisted approach to predict the dimensionality of lead iodide-based perovskites by analyzing the structure of an organic cation. Forde *et al.*[40] demonstrated that introducing organic spacer molecules with hole-acceptor states, such as naphthylethylammonium (NEA), can significantly reduce exciton binding energies in lead bromide perovskites. Understanding the scale of varying degrees of screening induced by different spacer molecules is critical to the modulation of optoelectronic properties of 2D perovskites.

Here, using the first-principles method, we attempt to reveal the dielectric screening effect of the spacer molecules on the optical properties and excitonic binding energy. Based

on the RP-type 2D perovskite, three typical spacer molecules, PMA, THMA and FUMA, are selected as representatives with different aromatic rings and dipoles. We find that, even with a simple modification in the aromatic organic ligands, for instance, the substitution of benzene in the PMA molecule with thiophene (THMA) and furan (FUMA), the interlayer coupling varies appreciably, inducing considerable Pb–I octahedral distortions. By calculating the formation energy and binding energy of perovskites, we reveal that the thiophene-based perovskite tends to have good stability. Through the calculation of local density of states (LDOS), thiophene is shown to have states closer to the band edge of perovskites, which is conducive to the migration of charge carriers. Moreover, by comparing the effective mass of charge carriers, dielectric constant and exciton binding energy from PSCs containing benzene ring ligands and furan ligands, we predict that perovskites with thiophene-based ligands have superior optoelectronic properties.

2. Computational methods

2.1. Density functional theory (DFT) calculations

We use the Vienna Ab Initio Simulation Package (VASP) code[55] for all calculations based on density functional theory.[56,57] The projector augmented wave (PAW)[58] was employed to describe the interaction between valence electrons and ion cores. Geometry optimization is carried out using the DFT-D2 method for the vdW-dispersion energy-correction term and Perdew–Burke–Ernzerhof (PBE) functional[59] under the generalized gradient approximation (GGA). Due to an underestimation of bandgaps by the PBE functional[60] and to capture self-interaction errors of electrons, the Heyd–Scuseria–Ernzerhof (HSE06) hybrid functional is used to calculate the electronic and optical properties, including the band structure, density of states, light absorption spectra, dielectric constants, and exciton binding energy. The geometric optimization and self-consistent field calculations are performed using the 3 × 3 × 1 and 4 × 4 × 1 *k*-mesh, respectively. The cutoff energy of the all plane wave basis set in the calculation is selected to be 400 eV. The atomic positions and lattice constants are fully relaxed until the maximum force is converged to 0.01 eV $Å^{-1}$.

2.2. Binding energy

Organic cations couple with adjacent inorganic layers through hydrogen-bonding interactions.[61] For the RP-type PSC, the inorganic octahedral layers and organic spacers are stabilized *via* electrostatic interactions between the charged A^+ ligands and octahedral PbI_4^{2-} units.[62] The electrostatic interactions of A_2PbI_4 can be evaluated based on the binding energy (E_B), which is derived as[35]

$$E_B = \frac{E_{A_2PbI_4} - E_{A_2^{2+}} - E_{PbI_4^{2-}}}{N} \quad (1)$$

where $E_{A_2PbI_4}$, $E_{A_2^{2+}}$ and $E_{PbI_4^{2-}}$ are the total energies of A_2PbI_4, A_2^{2+} and PbI_4^{2-}. N refers to the total atom number of the RP perovskite in the supercell. Here, E_B reflects the degree of cohesive interaction between the different charged components in the A_2PbI_4.

2.3. Formation energy

The formation energy has been widely used to characterize the chemical and thermodynamic stability of materials. Here, the stability of the perovskite is evaluated by the average formation energy (ΔH_{form}) per unit cell derived by comparing the energetics of the product (A_2PbI_4) and the reactants (AI and PbI_2):[63]

$$\Delta H_{form} = \frac{E_{A_2PbI_4} - 2E_{AI} - E_{PbI_2}}{N} \quad (2)$$

where $E_{A_2PbI_4}$, E_{AI}, E_{PbI_2} represent the total energies of A_2PbI_4, AI, PbI_2 per unit cell, respectively. N refers to the total atom number of the RP perovskite in the supercell.

2.4. Optical property

The light absorption coefficient α is defined as:

$$\alpha = \sqrt{2}\omega\left[\sqrt{\varepsilon_1(\omega)^2 + \varepsilon_2(\omega)^2} - \varepsilon_1(\omega)\right]^{1/2} \quad (3)$$

where ω, ε_1 and ε_2 refer to the frequency of incident light and real and imaginary parts of dielectric functions, respectively. The real (ε_1) and imaginary (ε_2) parts of the dielectric function were calculated using the frequency-dependent linear response method, as implemented in the VASP code.

2.5. Effective mass

The effective mass $m^*_{e/h}$ is derived from the following equation:

$$m^*_{e/h} = \hbar^2\left[\frac{\partial^2\varepsilon(k)}{\partial k^2}\right]^{-1} \quad (4)$$

where $\varepsilon(k)$ is the energy band close to VBM or CBM, and k is the wave vector along the transport direction. The effective mass of charge carriers can be obtained through parabolic fitting. m^*_r is the converted mass of charge carriers, which is the average of the converted masses of the electron effective mass and hole effective mass in both the XX and YY directions.[64]

$$m^*_r = \frac{\frac{m^*_{e,[XX]}m^*_{h,[XX]}}{m^*_{e,[XX]} + m^*_{h,[XX]}} + \frac{m^*_{e,[YY]}m^*_{h,[YY]}}{m^*_{e,[YY]} + m^*_{h,[YY]}}}{2} \quad (5)$$

3. Results and discussion

3.1. Effects of spacer molecules on lattice parameters

The chemical formula of the layered RP-phase perovskite is $A_2A'_{n-1}M_nX_{3n+1}$ (n = 1, 2, 3...), and A(A′) is an organic cation spacer molecule, such as butylammonium (BA^+) or 2-phenylethylammonium (PEA^+).[65] To examine the thickness effect of these materials, we have constructed monolayer and bilayer 2D RP perovskite models and added a vacuum layer with a thick-

ness of 15 Å along the *c*-axis to avoid the interaction between adjacent slabs. The crystal structures were modeled based on $(PMA)_2PbI_4$ [66] and the experimental structure of $(THMA)_2PbI_4$.[49] The $(FUMA)_2PbI_4$ model was derived by substituting the sulfur (S) in THMA with oxygen (O). The atomic structure of the RP perovskite is shown in Fig. 1; each Pb atom is bonded with six iodine atoms, forming an octahedron. The octahedra consisting of $[PbI_6]^{4-}$ groups are corner connected to form the 2D backbone layer. Negative charges in the lead-iodine layer are compensated by the organic cations, which are normally composed of methylamine cations (MA^+ = $-CH_2NH_3^+$) and benzene ($-C_6H_5$), thiophene ($-C_4H_3S$), or furan ($-C_4H_3O$) groups. Each monovalent organic cation forms a bond with each inorganic layer, and two adjacent inorganic layers are connected by vdW forces *via* the other end of the organic spacer molecules.

We first examine the effects of different organic cations on the lattice constants of monolayer and bilayer hybrid systems, which are listed in Table S1.† For $(PMA)_2PbI_4$ and $(THMA)_2PbI_4$, the lattice constant of the optimized bilayer HOIPs increases compared to that of the monolayer due to the interlayer interactions between adjacent organic layers.

The average Pb–I bond lengths of perovskites with different organic spacer molecules in both monolayer and bilayer structures are calculated and listed in Table S2.† Due to intra-molecular interactions amongst sizable cations in bilayer phases, stress arises, which induces lattice expansion, slightly elongating the horizontal Pb–I bonds in the bilayer system compared to the monolayer system. The choice of organic cations (*e.g.*, PMA, THMA, FUMA) influences the lattice constants and Pb–I bond lengths due to differences in molecular interactions. Changes in these parameters reflect alterations in the inorganic–organic layer coupling. Notably, a tiny substitution of the amine in the spacer molecule triggers an appreciable effect on the whole mixed compound, mainly attributable to the modulated spacer-inorganic layer interactions in the variant. For instance, due to the polarization effect of sulfur atoms, the methylamine group in THMA carries more positive charges than that of PMA, thus inducing a stronger affinity of the former with the iodine atoms of the inorganic octahedron. This leads to longer Pb–I bonds on the vertical equatorial plane for $(THMA)_2PbI_4$ compared to $(PMA)_2PbI_4$. Longer Pb–I bonds suggest stronger interactions between the organic cation and the inorganic framework, which can further modulate the lattice and stability. However, due to the larger electronegativity of oxygen atoms than sulfur atoms, FUMA exhibits stronger hydrogen bonding interactions with inorganic octahedra. This elongates the Pb–I bond perpendicular to the equatorial plane of the octahedron while shortening the Pb–I bond within the equatorial plane. Therefore, the bilayer $(FUMA)_2PbI_4$ lattice undergoes mild shrinkage compared to the backbone lattice of the monolayer. Overall, the structural changes induced by different organic cations, such as lattice expansion, lattice shrinkage, or bond elongation, could significantly influence material stability, optical properties, and quantum well effects. These variations modulate bandgaps and dielectric properties, ultimately impacting the material's performance in optoelectronic applications.

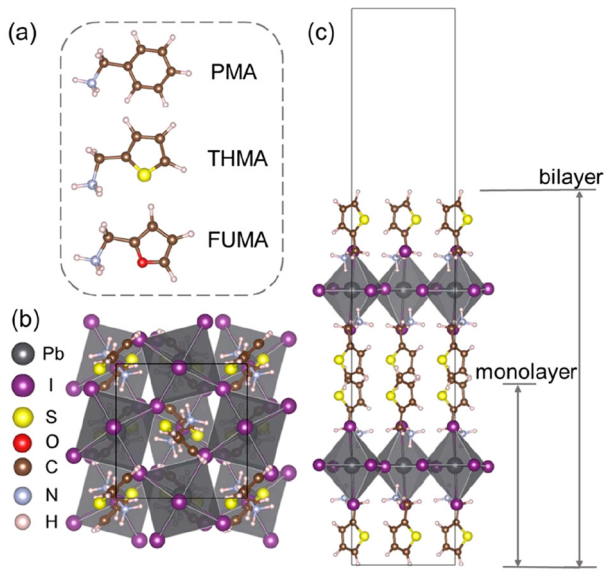

Fig. 1 (a) Three different organic spacer molecules differing from each other in the aromatic ring unit with a simple modification: phenyl methyl ammonium (PMA), thiophene methyl ammonium (THMA), and furan methyl ammonium (FUMA). (b) Atomic structure model of monolayer $(THMA)_2PbI_4$ as viewed along the *c*-axis. (c) Atomic structure model of $(THMA)_2PbI_4$ viewed along the side direction.

3.2. Adhesion energetics of spacer molecules with the inorganic layer

Our next attempt is to derive a quantitative estimation of the interaction between the various types of spacer molecules and lead iodide lattice. The formation energy ΔH_{form} and binding energy E_B for the monolayer and bilayer RP perovskites are examined. The ΔH_{form} of monolayer $(THMA)_2PbI_4$, $(FUMA)_2PbI_4$, and $(PMA)_2PbI_4$ is −0.052, −0.048, and −0.045 eV, respectively. The more negative value of ΔH_{form} of $(THMA)_2PbI_4$ suggests it is more energetically favorable and accordingly has a higher chance for good crystalline quality with respect to grain size and defect density than $(PMA)_2PbI_4$ and $(FUMA)_2PbI_4$. Larger domains and denser thin films are easier to obtain under lower values of ΔH_{form}. Experimental work confirmed that perovskites with unfavorable high ΔH_{form} are prone to defect formation.[67] Compounds with high ΔH_{form} are usually accompanied by disordered crystal structures, small crystal domains and random orientations, thus degrading the performance of perovskite devices. As compared in Fig. 2a, our work suggests that the $(THMA)_2PbI_4$ film, having the lowest ΔH_{form}, tends to have the highest quality.

The values of E_B of monolayer $(THMA)_2PbI_4$, $(FUMA)_2PbI_4$, and $(PMA)_2PbI_4$ are −0.138, −0.137, and −0.118 eV, respectively. $(THMA)_2PbI_4$ has the lowest E_B, suggesting a relatively strong interaction between THMA and the $[PbI_6]^{4-}$ octahedral component. This again indicates that $(THMA)_2PbI_4$ is the most stable. The same trend is found for both the monolayer and

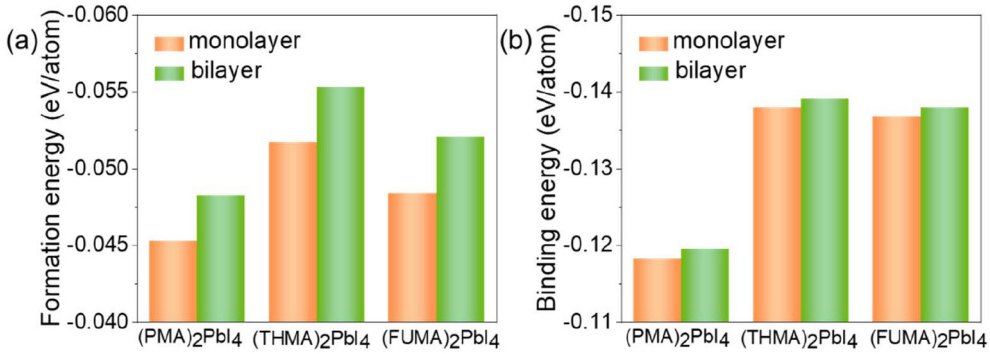

Fig. 2 (a) Formation energy (ΔH_{form}) and (b) binding energy (E_B) of three RP-phase $(PMA)_2PbI_4$, $(THMA)_2PbI_4$ and $(FUMA)_2PbI_4$ perovskites in the monolayer and bilayer forms.

bilayers. The E_B of the bilayer perovskites is slightly more favorable than that of the monolayer. This would be related to the dipolar interactions, as noncovalent interactions between large cations, which can affect the ΔH_{form} and E_B. We find that introducing sulfur or oxygen atoms in spacer molecules, as in the cases of THMA and FUMA, respectively, increases the dipole moment of the organic spacer molecules. This enhancement in dipole moment strengthens the interaction between inorganic plates and organic layers. As a result, slightly more favorable bindings are formed in $(THMA)_2PbI_4$ and $(FUMA)_2PbI_4$ between the organic layer and the Pb–I layer.

3.3. Octahedral tilt and electronic properties with different spacer molecules

In this section, we study the function of spacer molecules and their role in affecting the overall electronic properties of perovskites. The electronic band structures of $(PMA)_2PbI_4$, $(THMA)_2PbI_4$, and $(FUMA)_2PbI_4$ calculated using HSE06 are shown in Fig. 3. All the perovskites we examined, regardless of different thicknesses and organic ligands, have a direct band gap with the conduction band minimum (CBM) and the valence band maximum (VBM) residing at the Γ point of the Brillouin zone. The band gaps of monolayer $(PMA)_2PbI_4$, $(THMA)_2PbI_4$ and $(FUMA)_2PbI_4$ are 2.66, 2.75 and 2.76 eV, respectively, and the band gaps of the bilayer are almost the same as the monolayer counterparts as 2.65, 2.73 and 2.78 eV, respectively. It should be noted that the band gap of 2D HOIPs is determined by the degree of overlap of metals and halides in the inorganic network.[68] When the bond angle of Pb–I–Pb is 180°, the distortion of the octahedron is the weakest; hence, the orbital overlap of Pb and I atoms is at its maximum, and the band gap of the HOIP is the narrowest.[69] However, in real situations, due to the hydrogen bonding effect of methylamine and halide, the in-plane tilt and out-of-plane tilt of $[PbI_6]^{4-}$

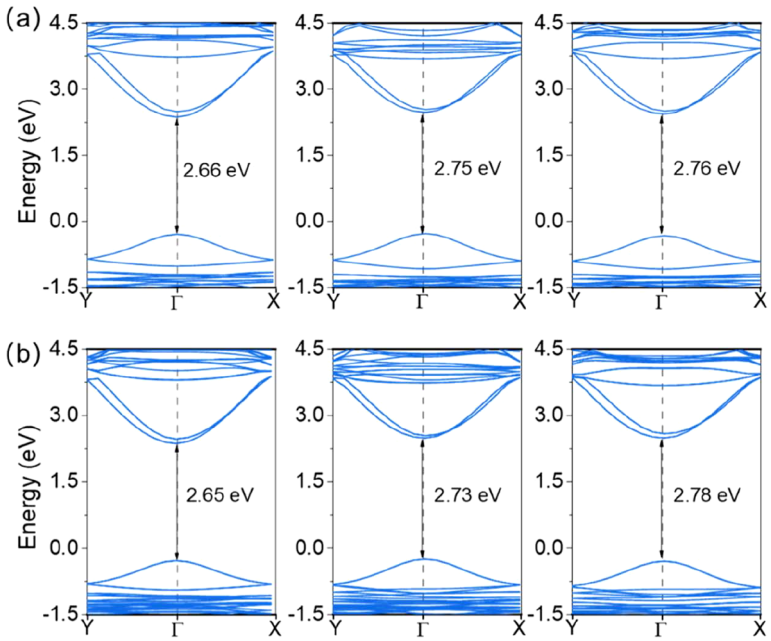

Fig. 3 Band structures (calculated using HSE06) of (a) monolayer and (b) bilayer RP-phase $(PMA)_2PbI_4$, $(THMA)_2PbI_4$ and $(FUMA)_2PbI_4$ perovskites.

octahedron make the band gap of organic–inorganic perovskite larger than the ideal situation.[70] Here, we use the average Pb–I–Pb bond angle and I–I–I bond angle to signify the degree of out-of-plane and in-plane tilt, respectively, and we list the average bond angles of different systems in Table S2.† Additionally, the Pb–I–Pb and I–I–I bond angles are highlighted in the enlarged figures and views along the *c*-axis provided in Fig. S1–S6,† which offer a detailed visualization of these angles in different systems. It is observed that the Pb–I–Pb and I–I–I bond angles of monolayer $(PMA)_2PbI_4$ are 153° and 116°, and those of the bilayer are 155° and 114°, respectively. Therefore, the octahedral distortion in the bilayer is slightly weaker than in the monolayer. Compared with $(THMA)_2PbI_4$ and $(FUMA)_2PbI_4$, $(PMA)_2PbI_4$ has the weakest out-of-plane distortion and in-plane distortion, and hence the narrowest band gap.

In contrast, the Pb–I–Pb and I–I–I bond angles of monolayer $(FUMA)_2PbI_4$ are 149° and 121°, while those of the bilayer $(FUMA)_2PbI_4$ are 147° and 123°, respectively, showing larger distortion in the bilayer, opposite to that of $(PMA)_2PbI_4$. The larger distortion of the octahedron triggered in the bilayer $(FUMA)_2PbI_4$ is responsible for the larger band gap of the bilayer $(FUMA)_2PbI_4$ than that of the monolayer. To further quantify the internal distortions of the octahedra, we calculated the average octahedral angle variance ($\sigma_{oct}{}^2$), average octahedron distortion parameter (Δ),[71] and average quadratic elongation ($\langle\lambda\rangle$),[72] as shown in Table S3.† While the trends in $\sigma_{oct}{}^2$ show a slight increase from monolayer to bilayer systems, the distortion parameter (Δ) and quadratic elongation ($\langle\lambda\rangle$) align well with the tilt trends. For instance, in $(PMA)_2PbI_4$, Δ and $\langle\lambda\rangle$ decrease in the bilayer, indicating reduced internal bond length distortions and improved structural stability. It is worth noting that the adjacent organic layers are not simply stacked above each other, but permeate into each other with molecules interlocked. Therefore, when perovskite changes from monolayer to bilayer, the thickness of the $(PMA)_2PbI_4$ with the deepest penetration depth, opposite to common notion, reduces from 16.61 Å to 15.45 Å. The overlap between organic layers can reduce the distance between adjacent inorganic layers while also reducing the barrier of multiple quantum wells.[73] The differences in band gaps caused by organic ligands, therefore, indicate that the band gaps can be tuned by a selective design of the organic ligands. Nevertheless, changes in thickness only affect the value of the band gap and do not affect the dispersion of the band structure; in other words, the selection rule and path of quantum scattering processes are largely maintained. As shown in Table 1, there is no obvious change in the calculated effective mass of systems with different thicknesses, and all three types of perovskites have comparable effective masses for both electrons and holes.

Distribution of the respective electronic states of Pb, I and spacer molecules in the valence band and conduction band can be seen from LDOS, which is shown in Fig. 4. The LDOS profiles of $(PMA)_2PbI_4$, $(THMA)_2PbI_4$, and $(FUMA)_2PbI_4$ are similar. The CBM and VBM are mainly contributed by Pb and I, respectively, suggesting that conducting electrons and holes are mainly distributed on lead and iodine atoms, respectively. In contrast, the organic cations have no contribution around CBM and VBM and thus are not directly responsible for carrier concentration and transport. The organic spacer molecules are involved *via* an indirect way by distorting or tilting the $[PbI_6]^{4-}$ octahedron.

Nevertheless, the states of organic spacer molecules are located around 0.83 eV below the VBM and 1.50 eV above the CBM in monolayer RP perovskite and 0.26 eV below the VBM and 1.34 eV above the CBM in bilayer RP perovskite, suggesting that they are highly likely to be involved in the relaxation of hot-carriers. In monolayer RP perovskite, the levels of THMA are closer to band edges than those in PMA, which reflects that the π orbital of the conjugated group of thiophene has a higher energy than that of benzene. Meanwhile, the π orbital of the thiophene is less stabilized than that of benzene, thus inducing better conductivity of the former. Similarly, compared with PMA, the peak of FUMA is located closer to the VBM, which is conducive to hole injection and transport between the organic and inorganic layers. For the bilayer perovskites, the overlapping states of organic cations make all the occupied states of the organic molecules move towards the VBM, indicating that the interaction between organic layers can make the conjugated structure more active. Acting as the tunneling mediating center, the coupled conjugated spacer molecules in multilayer PSCs improve the conductivity and transport of interlayer carriers.

3.4. Dielectrics, exciton binding energy and optical absorption

Finally, we would like to examine the screening effect of these spacer molecules with different aromatic derivatives by analyzing the dielectric properties. As shown in Fig. 5, the frequency-dependent dielectric function with both real and complex components is plotted. Table 2 provides the optical dielectric

Table 1 Effective mass *m** and converted mass m_r^* of electron (e) and hole (h) in units of free-electron mass in RP-phase $(PMA)_2PbI_4$, $(THMA)_2PbI_4$ and $(FUMA)_2PbI_4$ perovskites

		$m^*_{h,[XX]}$	$m^*_{h,[YY]}$	$m^*_{e,[XX]}$	$m^*_{e,[YY]}$	m_r^*
Monolayer	$(PMA)_2PbI_4$	0.60	0.56	0.39	0.51	0.25
	$(THMA)_2PbI_4$	0.57	0.58	0.39	0.60	0.26
	$(FUMA)_2PbI_4$	0.59	0.60	0.39	0.60	0.27
Bilayer	$(PMA)_2PbI_4$	0.63	0.58	0.39	0.49	0.25
	$(THMA)_2PbI_4$	0.58	0.58	0.38	0.57	0.26
	$(FUMA)_2PbI_4$	0.59	0.61	0.41	0.63	0.28

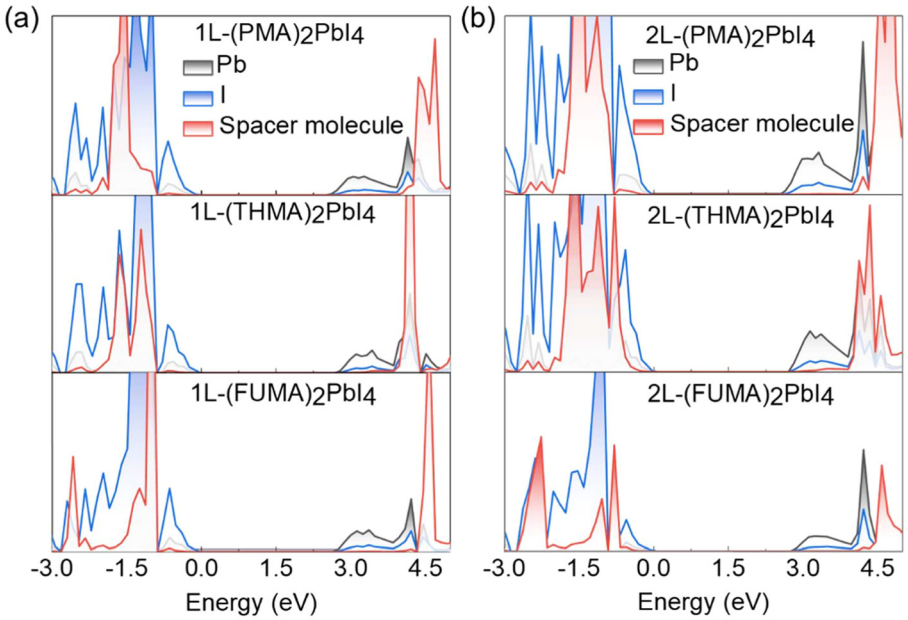

Fig. 4 LDOS of (a) monolayer and (b) bilayer RP-phase $(PMA)_2PbI_4$, $(THMA)_2PbI_4$ and $(FUMA)_2PbI_4$ perovskites with three different ligands.

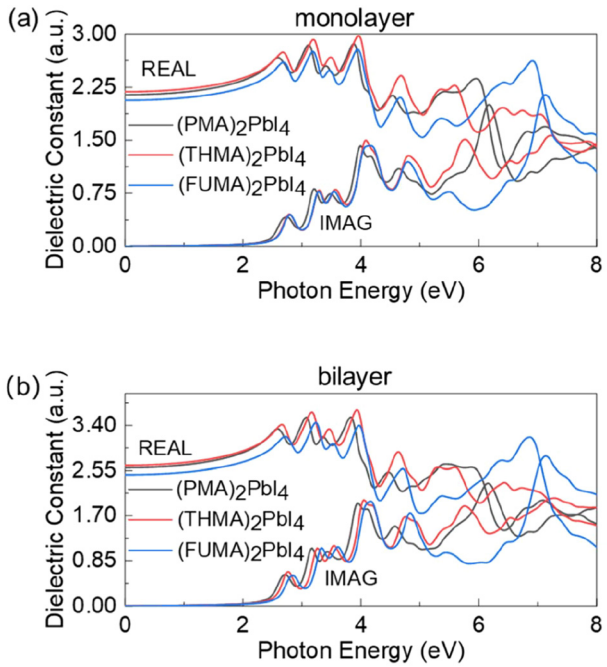

Fig. 5 Real and imaginary dielectric constants of (a) monolayer and (b) bilayer RP-phase $(PMA)_2PbI_4$, $(THMA)_2PbI_4$ and $(FUMA)_2PbI_4$ perovskites.

constants and exciton binding energies E_b, which are calculated using the Wannier exciton model:[74]

$$E_b = \frac{m_e e^4}{2(4\pi\varepsilon_0)^2\hbar^2}\frac{m_r^*}{m_e}\frac{1}{\varepsilon_\infty{}^2}\frac{1}{a^2} \approx 13.56\frac{m_r^*}{m_e}\frac{1}{\varepsilon_\infty{}^2}\frac{1}{a^2} \quad (6)$$

where m_e is the electron mass, ε_∞ is the optical dielectric constant calculated using density functional perturbation theory, a is exciton energy level and m_r^* is the converted mass of charge carriers.

In the monolayer limit, the optical dielectric constants of $(FUMA)_2PbI_4$, $(PMA)_2PbI_4$, and $(THMA)_2PbI_4$ are 2.07, 2.14 and 2.20, respectively, while the values increase to 2.47, 2.60 and 2.65 for the bilayer compounds, respectively. Overall, all three types of perovskites exhibit a relatively high E_b of exciton. With the highest dielectric constant, $(THMA)_2PbI_4$ has the lowest E_b, with 739 meV and 499 meV in the monolayer and bilayer cases, respectively. The E_b of the bilayer system is lower than that of the monolayer system because of a larger dielectric constant and thus a stronger screening effect in the former. The higher exciton E_b in the monolayer implies that electrons and holes recombine easily and are difficult to separate.[75]

The RP-type perovskites consist of alternating layers of insulating spacer molecules and layers of inorganic octahedral, forming perfect intrinsic multiple quantum well structures. In the stacked 2D heterostructure, the dielectric mismatch between the organic and inorganic layer facilitates exciton binding, raising additional energy for separating excitons into free charges.[76] This degrades the ability to utilize light and suppresses the solar-to-carrier efficiency. Fortunately, a proper introduction of spacer cations with sizable dipole moments can regulate dielectric confinement and mitigate this issue. For instance, differing from PMA and FUMA molecules, THMA with a relatively high dipole moment improves carrier dissociation, indicating the lowest E_b of the exciton. This indicates that the dielectric confinement of layered 2D perovskite structures can be adjusted by designing A-site large cations.

The optical and dielectric properties of HOIP, in fact, are dictated by many factors, such as the spacer molecule features and distortion of octahedra. As shown in Fig. 6, despite a tiny difference in the aromatic ring of the three spacer molecules,

Table 2 Relative optical dielectronic constant (ε_∞) and exciton binding energy (E_b) and band gap (E_g) of monolayer and bilayer $(PMA)_2PbI_4$, $(THMA)_2PbI_4$ and $(FUMA)_2PbI_4$ perovskites

		ε_∞	E_b (meV)	E_g (eV)
Monolayer	$(PMA)_2PbI_4$	2.14	741	2.66
	$(THMA)_2PbI_4$	2.20	739	2.75
	$(FUMA)_2PbI_4$	2.07	849	2.76
Bilayer	$(PMA)_2PbI_4$	2.60	505	2.65
	$(THMA)_2PbI_4$	2.65	499	2.73
	$(FUMA)_2PbI_4$	2.47	612	2.78

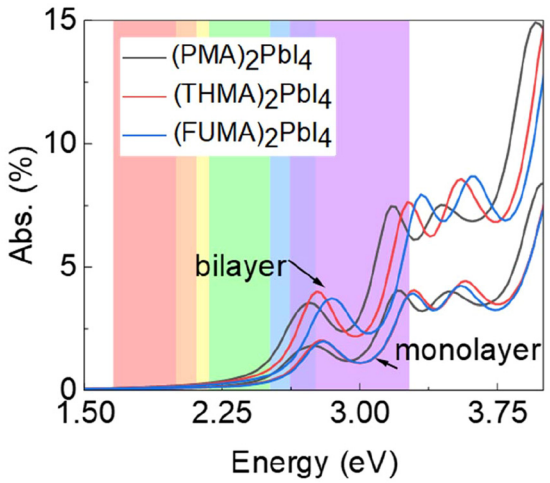

Fig. 6 Optical absorption spectra of (a) monolayer and (b) bilayer RP-phase $(PMA)_2PbI_4$, $(THMA)_2PbI_4$ and $(FUMA)_2PbI_4$ perovskites.

the three RP perovskite derivatives undergo a clear shift in the absorption spectrum, and the difference is more prominent in the thick bilayer material compared with the monolayer. Substitution of a carbon atom in the benzene of the PMA molecule with the sulfur in THMA and oxygen in FUMA induces a blue shift of absorption, in line with the previous electronic band structures. As expected, the light absorption coefficient of bilayer systems is generally larger than that of the monolayer systems.

Actually, many studies have been devoted to using spacer molecules containing thiophene functional groups to modulate optoelectronic performance. Incorporating THMA spacer groups effectively induces crystal growth with preferential vertical growth orientations and hinders ionic motion, thereby improving carrier lifetimes and reducing recombination losses with the PCE up to 21.49%.[77] Qin *et al.* demonstrated that $(TEA)_2(MA)_2Pb_3I_{10}$(TEA = 2-thiophene ethylamine) thin films have a narrow distribution and preferred vertical crystal orientation,[78] significantly improving photovoltaic performance and reproducibility, retaining over 93% of the original PCE under ambient air and illumination conditions. Dong *et al.* synthesized 2D $(THFA)_2(MA)_2Pb_3I_{10}$(THFA = 2-thiopheneformamidinium) films with a PCE of 16.72% and a significant overall stability.[79] After precursor organic salts-assisted crystal growth (PACG) method treatment, the grain size of the $(THFA)_2(MA)_2Pb_3I_{10}$ thin film increases, together with reduced grain boundaries and trap density, resulting in elongated carrier lifetimes and suppressed nonradiative recombination losses. The improvement in stability is consistent with our results of compact lattice and enhanced stability by the thiophene group.

4. Conclusions

In this work, through first-principles calculations, we explore the influence of spacer molecules in 2D-RP perovskites by tailoring conjugated aromatic units while maintaining their geometric shapes. Our results reveal that the modest modification of the aromatic benzene ring of the spacer molecules, as indicated by the three typical spacer molecules PMA, THMA and FUMA, can induce a sizable effect on the perovskite properties. The most prominent change would be the tailored interlayer coupling, thus regulating the formation energy of the HOIPs. The spacer molecules with different functional groups also impose different tilts of Pb–I octahedra and accordingly modify the band gaps. Importantly, the various molecules can induce different screening effects by varying the macroscopic dielectric constant of the compounds. For instance, $(THMA)_2PbI_4$ perovskite with THMA has a relatively high dielectric constant, which can mitigate the dielectric mismatch and suppress carrier recombination. Our work suggests the prominent role of the engineering of the spacer molecules in modulating the stability, quality of grown films and electronic properties of inorganic–organic 2D perovskites.

Data availability

The data supporting this article have been included as part of the ESI.†

Conflicts of interest

There are no conflicts to declare.

Acknowledgements

This work is supported by the Natural Science Foundation of Guangdong Province, China (2024A1515011161), and the Science and Technology Development Fund from Macau SAR (FDCT-0163/2019/A3, 0085/2023/ITP2, 0120/2023/RIA2). This work was performed in part at the High-Performance Computing Cluster (HPCC), which is supported by the Information and Communication Technology Office (ICTO) of the University of Macau.

References

1 J. B. Patel, A. D. Wright, K. B. Lohmann, K. Peng, C. Q. Xia, J. M. Ball, N. K. Noel, T. W. Crothers, J. Wong-Leung, H. J. Snaith, L. M. Herz and M. B. Johnston, *Adv. Energy Mater.*, 2020, **10**, 1903653.

2 A. Liang, Y. Gao, R. Asadpour, Z. Wei, B. P. Finkenauer, L. Jin, J. Yang, K. Wang, K. Chen, P. Liao, C. Zhu, L. Huang, B. W. Boudouris, M. A. Alam and L. Dou, *J. Am. Chem. Soc.*, 2021, **143**, 15215–15223.

3 S. Shrestha, X. Li, H. Tsai, C.-H. Hou, H.-H. Huang, D. Ghosh, J.-J. Shyue, L. Wang, S. Tretiak, X. Ma and W. Nie, *Chem*, 2022, **8**, 1107–1120.

4 J. Zhang, S. Tang, M. Zhu, Z. Li, Z. Cheng, S. Xiang and Z. Zhang, *Energy Environ. Mater.*, 2024, e12696.

5 Q. Tao, P. Xu, M. Li and W. Lu, *npj Comput. Mater.*, 2021, **7**, 23.

6 J. Y. Kim, J.-W. Lee, H. S. Jung, H. Shin and N.-G. Park, *Chem. Rev.*, 2020, **120**, 7867–7918.

7 A. Fakharuddin, M. K. Gangishetty, M. Abdi-Jalebi, S.-H. Chin, A. R. Bin Mohd Yusoff, D. N. Congreve, W. Tress, F. Deschler, M. Vasilopoulou and H. J. Bolink, *Nat. Electron.*, 2022, **5**, 203–216.

8 S. P. Senanayak, M. Abdi-Jalebi, V. S. Kamboj, R. Carey, R. Shivanna, T. Tian, G. Schweicher, J. Wang, N. Giesbrecht, D. Di Nuzzo, H. E. Beere, P. Docampo, D. A. Ritchie, D. Fairen-Jimenez, R. H. Friend and H. Sirringhaus, *Sci. Adv.*, 2020, **6**, eaaz4948.

9 H. Yu, X. Xu, H. Liu, Y. Wan, X. Cheng, J. Chen, Y. Ye and L. Dai, *ACS Nano*, 2020, **14**, 552–558.

10 L. Pan, S. Shrestha, N. Taylor, W. Nie and L. R. Cao, *Nat. Commun.*, 2021, **12**, 5258.

11 A. Kojima, K. Teshima, Y. Shirai and T. Miyasaka, *J. Am. Chem. Soc.*, 2009, **131**, 6050–6051.

12 **https://www.nrel.gov/pv/interactive-cell-efficiency.html**.

13 J. M. Hoffman, I. Hadar, X. Li, W. Ke, E. S. Vasileiadou, J. Strzalka, L. X. Chen and M. G. Kanatzidis, *Chem*, 2022, **8**, 1067–1082.

14 Z. Chen, G. Brocks, S. Tao and P. A. Bobbert, *Nat. Commun.*, 2021, **12**, 2687.

15 J. Jeong, M. Kim, J. Seo, H. Lu, P. Ahlawat, A. Mishra, Y. Yang, M. A. Hope, F. T. Eickemeyer, M. Kim, Y. J. Yoon, I. W. Choi, B. P. Darwich, S. J. Choi, Y. Jo, J. H. Lee, B. Walker, S. M. Zakeeruddin, L. Emsley, U. Rothlisberger, A. Hagfeldt, D. S. Kim, M. Grätzel and J. Y. Kim, *Nature*, 2021, **592**, 381–385.

16 N. Mussakhanuly, E. Choi, R. L. Chin, Y. Wang, J. Seidel, M. A. Green, A. M. Soufiani, X. Hao and J. S. Yun, *ACS Appl. Mater. Interfaces*, 2024, **16**, 7961–7972.

17 Y. Zhang, Y. Liu and S. F. Liu, *Adv. Funct. Mater.*, 2023, **33**, 2210335.

18 D. Xu, J. Wang, Y. Duan, S. Yang, H. Zou, L. Yang, N. Zhang, H. Zhou, X. Lei, M. Wu, S. Liu and Z. Liu, *Adv. Funct. Mater.*, 2023, **33**, 2304237.

19 C. Han, Y. Wang, J. Yuan, J. Sun, X. Zhang, C. Cazorla, X. Wu, Z. Wu, J. Shi, J. Guo, H. Huang, L. Hu, X. Liu, H. Y. Woo, J. Yuan and W. Ma, *Angew. Chem., Int. Ed.*, 2022, **61**, e202205111.

20 H. Chen, Q. Guan, H. Yan, X. Cui, Z. Shu and Y. Cai, *ACS Appl. Mater. Interfaces*, 2023, **15**, 32475–32486.

21 H. Chen, H. Yan and Y. Cai, *J. Mater. Chem. A*, 2023, **11**, 19349–19359.

22 H. Chen, H. Yan and Y. Cai, *Chem. Mater.*, 2022, **34**, 1020–1029.

23 Y. Xu, M. Wang, Y. Lei, Z. Ci and Z. Jin, *Adv. Energy Mater.*, 2020, **10**, 2002558.

24 Y. Zhang, M. Chen, T. He, H. Chen, Z. Zhang, H. Wang, H. Lu, Q. Ling, Z. Hu, Y. Liu, Y. Chen and G. Long, *Adv. Mater.*, 2023, **35**, 2210836.

25 H. Yao, T. Wu, C. Wu, L. Ding, Y. Hua and F. Hao, *Adv. Funct. Mater.*, 2024, **34**, 2312287.

26 Y. Qian, J. Li, H. Cao, Z. Ren, X. Dai, T. Huang, S. Zhang, Y. Qiu, L. Yang and S. Yin, *Adv. Funct. Mater.*, 2023, **33**, 2214731.

27 B. Kim and S. I. Seok, *Energy Environ. Sci.*, 2020, **13**, 805–820.

28 X. Zhao, T. Liu and Y. L. Loo, *Adv. Mater.*, 2022, **34**, 2105849.

29 J. Zhang, J. Wu, S. Langner, B. Zhao, Z. Xie, J. A. Hauch, H. A. Afify, A. Barabash, J. Luo, M. Sytnyk, W. Meng, K. Zhang, C. Liu, A. Osvet, N. Li, M. Halik, W. Heiss, Y. Zhao and C. J. Brabec, *Adv. Funct. Mater.*, 2022, **32**, 2207101.

30 B. Zhang, Z. Xu, C. Ma, H. Li, Y. Liu, L. Gao, J. Zhang, J. You and S. F. Liu, *Adv. Funct. Mater.*, 2022, **32**, 2110392.

31 R. Lin, J. Xu, M. Wei, Y. Wang, Z. Qin, Z. Liu, J. Wu, K. Xiao, B. Chen, S. M. Park, G. Chen, H. R. Atapattu, K. R. Graham, J. Xu, J. Zhu, L. Li, C. Zhang, E. H. Sargent and H. Tan, *Nature*, 2022, **603**, 73–78.

32 Z. Zhang, L. Qiao, K. Meng, R. Long, G. Chen and P. Gao, *Chem. Soc. Rev.*, 2023, **52**, 163–195.

33 A. A. O. El-Ballouli, O. M. Bakr and O. F. Mohammed, *J. Phys. Chem. Lett.*, 2020, **11**, 5705–5718.

34 S. Tao, I. Schmidt, G. Brocks, J. Jiang, I. Tranca, K. Meerholz and S. Olthof, *Nat. Commun.*, 2019, **10**, 2560.

35 Q. Sun, Z. Fang, Y. Zheng, Z. Yang, F. Hu, Y. Yang, W. Yang, X. Hou and M.-H. Shang, *J. Mater. Chem. A*, 2022, **10**, 3996–4005.

36 L. Yan, J. Ma, P. Li, S. Zang, L. Han, Y. Zhang and Y. Song, *Adv. Mater.*, 2022, **34**, 2106822.

37 S. Peng, J. Ma, P. Li, S. Zang, Y. Zhang and Y. Song, *Adv. Funct. Mater.*, 2022, **32**, 2205289.

38 J. Liang, Z. Zhang, Q. Xue, Y. Zheng, X. Wu, Y. Huang, X. Wang, C. Qin, Z. Chen and C.-C. Chen, *Energy Environ. Sci.*, 2022, **15**, 296–310.

39 A. Simbula, L. Wu, F. Pitzalis, R. Pau, S. Lai, F. Liu, S. Matta, D. Marongiu, F. Quochi, M. Saba, A. Mura and G. Bongiovanni, *Nat. Commun.*, 2023, **14**, 4125.

40 A. Forde, S. Tretiak and A. J. Neukirch, *Nano Lett.*, 2023, **23**, 11586–11592.

41 M. C. Gélvez-Rueda, M. B. Fridriksson, R. K. Dubey, W. F. Jager, W. Van Der Stam and F. C. Grozema, *Nat. Commun.*, 2020, **11**, 1901.

42 Q. Fu, M. Chen, Q. Li, H. Liu, R. Wang and Y. Liu, *J. Am. Chem. Soc.*, 2023, **145**, 21687–21695.
43 X. Gan, W. Zhao, T. Xu, Y. Liang, L. Guo and H. Liu, *J. Mater. Sci.*, 2021, **56**, 17167–17177.
44 M. E. Kamminga, H.-H. Fang, M. R. Filip, F. Giustino, J. Baas, G. R. Blake, M. A. Loi and T. T. M. Palstra, *Chem. Mater.*, 2016, **28**, 4554–4562.
45 G. Yan, G. Sui, W. Chen, K. Su, Y. Feng and B. Zhang, *Chem. Mater.*, 2022, **34**, 3346–3356.
46 J. Liang, Z. Zhang, Y. Huang, Q. Xue, Y. Zheng, X. Wu, C. Tian, Y. Zhang, Y. Wang, Z. Chen and C. C. Chen, *Adv. Funct. Mater.*, 2022, **32**, 2207177.
47 H. Lai, B. Kan, T. Liu, N. Zheng, Z. Xie, T. Zhou, X. Wan, X. Zhang, Y. Liu and Y. Chen, *J. Am. Chem. Soc.*, 2018, **140**, 11639–11646.
48 H. Lai, D. Lu, Z. Xu, N. Zheng, Z. Xie and Y. Liu, *Adv. Mater.*, 2020, **32**, 2001470.
49 C. Ni, Y. Huang, T. Zeng, D. Chen, H. Chen, M. Wei, A. Johnston, A. H. Proppe, Z. Ning, E. H. Sargent, P. Hu and Z. Yang, *Angew. Chem.*, 2020, **132**, 14081–14087.
50 Y. Zheng, S.-C. Chen, Y. Ma and Q. Zheng, *Sol. RRL*, 2022, **6**, 2200221.
51 R. Wang, X. Dong, Q. Ling, Q. Fu, Z. Hu, Z. Xu, H. Zhang, Q. Li and Y. Liu, *ACS Energy Lett.*, 2022, **7**, 3656–3665.
52 E. I. Marchenko, S. A. Fateev, A. A. Petrov, V. V. Korolev, A. Mitrofanov, A. V. Petrov, E. A. Goodilin and A. B. Tarasov, *Chem. Mater.*, 2020, **32**, 7383–7388.
53 X. Lu, C. Stoumpos, Q. Hu, X. Ma, D. Zhang, S. Guo, J. Hoffman, K. Bu, X. Guo, Y. Wang, C. Ji, H. Chen, H. Xu, Q. Jia, W. Yang, M. G. Kanatzidis and H. K. Mao, *Natl. Sci. Rev.*, 2021, **8**, nwaa288.
54 R. Lyu, C. E. Moore, T. Liu, Y. Yu and Y. Wu, *J. Am. Chem. Soc.*, 2021, **143**, 12766–12776.
55 G. Kresse and J. Furthmuller, *Phys. Rev. B: Condens. Matter Mater. Phys.*, 1996, **54**, 11169–11186.
56 W. Kohn and L. J. Sham, *Phys. Rev.*, 1965, **140**, A1133–A1138.
57 P. Hohenberg and W. Kohn, *Phys. Rev.*, 1964, **136**, B864–B871.
58 P. E. Blöchl, *Phys. Rev. B: Condens. Matter Mater. Phys.*, 1994, **50**, 17953–17979.
59 J. P. Perdew, K. Burke and M. Ernzerhof, *Phys. Rev. Lett.*, 1996, **77**, 3865–3868.
60 J. Heyd, G. E. Scuseria and M. Ernzerhof, *J. Chem. Phys.*, 2006, **124**, 8207.
61 Y. Zhong, G. Liu, Y. Su, W. Sheng, L. Gong, J. Zhang, L. Tan and Y. Chen, *Angew. Chem., Int. Ed.*, 2022, **134**, e202114588.
62 F. El-Mellouhi, A. Marzouk, E. T. Bentria, S. N. Rashkeev, S. Kais and F. H. Alharbi, *ChemSusChem*, 2016, **9**, 2648–2655.
63 Y. Yang, F. Gao, S. Gao and S.-H. Wei, *J. Mater. Chem. A*, 2018, **6**, 14949–14955.
64 G.-M. Sui, G.-J. Yan, G. Yang, B. Zhang, Y.-Q. Feng and T. U. School of Chemical Engineering and Technology, Tianjin 300350, China and T. U. Tianjin Co-Innovation Center of Chemical Science and Engineering, Tianjin 300720, China, *Acta Phys. Sin.*, 2022, **71**, 208801.
65 R. Chiara, M. Morana, M. Boiocchi, M. Coduri, M. Striccoli, F. Fracassi, A. Listorti, A. Mahata, P. Quadrelli, M. Gaboardi, C. Milanese, L. Bindi, F. De Angelis and L. Malavasi, *J. Mater. Chem. C*, 2021, **9**, 9899–9906.
66 M.-H. Tremblay, J. Bacsa, B. Zhao, F. Pulvirenti, S. Barlow and S. R. Marder, *Chem. Mater.*, 2019, **31**, 6145–6153.
67 P. Liu, N. Han, W. Wang, R. Ran, W. Zhou and Z. Shao, *Adv. Mater.*, 2021, **33**, 2002582.
68 D. Ghosh, D. Acharya, L. Pedesseau, C. Katan, J. Even, S. Tretiak and A. J. Neukirch, *J. Mater. Chem. A*, 2020, **8**, 22009–22022.
69 Y. Shao, W. Gao, H. Yan, R. Li, I. Abdelwahab, X. Chi, L. Rogée, L. Zhuang, W. Fu, S. P. Lau, S. F. Yu, Y. Cai, K. P. Loh and K. Leng, *Nat. Commun.*, 2022, **13**, 138.
70 A. Pisanu, M. Coduri, M. Morana, Y. O. Ciftci, A. Rizzo, A. Listorti, M. Gaboardi, L. Bindi, V. I. E. Queloz, C. Milanese, G. Grancini and L. Malavasi, *J. Mater. Chem. A*, 2020, **8**, 1875–1886.
71 X. B. Han, C. Q. Jing, H. Y. Zu and W. Zhang, *J. Am. Chem. Soc.*, 2022, **144**, 18595–18606.
72 X. Li, Y. Guan, X. Li and Y. Fu, *J. Am. Chem. Soc.*, 2022, **144**, 18030–18042.
73 Y. Yao, D. Cao, J. Yan, M. Zhang, X. Chen and H. Shu, *J. Phys. Chem. C*, 2022, **126**, 8408–8416.
74 U.-G. Jong, C.-J. Yu, J.-S. Ri, N.-H. Kim and G.-C. Ri, *Phys. Rev. B*, 2016, **94**, 125139.
75 J. H. Bombile, M. J. Janik and S. T. Milner, *Phys. Chem. Chem. Phys.*, 2019, **21**, 11999–12011.
76 J. V. Passarelli, C. M. Mauck, S. W. Winslow, C. F. Perkinson, J. C. Bard, H. Sai, K. W. Williams, A. Narayanan, D. J. Fairfield, M. P. Hendricks, W. A. Tisdale and S. I. Stupp, *Nat. Chem.*, 2020, **12**, 672–682.
77 T. Zhou, H. Lai, T. Liu, D. Lu, X. Wan, X. Zhang, Y. Liu and Y. Chen, *Adv. Mater.*, 2019, 1901242.
78 Y. Qin, H. Zhong, J. J. Intemann, S. Leng, M. Cui, C. Qin, M. Xiong, F. Liu, A. K. Y. Jen and K. Yao, *Adv. Energy Mater.*, 2020, **10**, 1904050.
79 Y. Dong, D. Lu, Z. Xu, H. Lai and Y. Liu, *Adv. Energy Mater.*, 2020, **10**, 2000694.